Published in final edited form as:

ACS Appl Mater Interfaces. 2021 September 01; 13(34): 40379–40391. doi:10.1021/acsami.1c11791.

Bimodal Nanocomposite Platform with Antibiofilm and Self-Powering Functionalities for Biomedical Applications

Atul Dhall[1], **Sayemul Islam**[2], **Moonchul Park**[2], **Yu Zhang**[1,3], **Albert Kim**[2,*], **Geelsu Hwang**[1,3,*]

[1]Department of Preventive and Restorative Sciences, School of Dental Medicine, University of Pennsylvania, Philadelphia, PA 19104, USA

[2]Department of Electrical and Computer Engineering, Temple University, Philadelphia, PA 19122, USA

[3]Center for Innovation & Precision Dentistry, School of Dental Medicine, School of Engineering and Applied Sciences, University of Pennsylvania, Philadelphia, PA 19104, USA

Abstract

Advances in microelectronics and nanofabrication have led to the development of implantable biomaterials. However, biofilm-associated infection on medical devices is a major hurdle that substantially undermines the clinical applicability and advancement of biomaterial systems. Given their attractive piezoelectric behavior, BTO-based materials have also been used in biological applications. Despite its versatility, the feasibility of BTO-embedded biomaterials as anti-infectious implantable medical devices in the human body has not been explored yet. Here, the first demonstration of clinically viable BTO-nanocomposites is presented. It demonstrates potent antibiofilm properties against *Streptococcus mutans* without bactericidal effect while retaining their piezoelectric and mechanical behaviors. This anti-adhesive effect led to >10-fold reduction in colony-forming units *in vitro*. To elucidate the underlying mechanism for this effect, data depicting unfavorable interaction energy profiles between BTO-nanocomposites and *S. mutans* using the extended-Derjaguin, Landau, Verwey, and Overbeek theory is presented. Direct cell-to-surface binding force data using atomic force microscopy also corroborate reduced adhesion between BTO-nanocomposites and *S. mutans*. Interestingly, poling process on BTO-nanocomposites resulted in asymmetrical surface charge density on each side, which may help tackle two major issues in prosthetics- bacterial contamination and tissue integration. Finally, BTO-nanocomposites exhibit superior biocompatibility towards human gingival fibroblasts and keratinocytes. Overall, BTO-embedded composites exhibit the broad-scale potential to be used in biological settings as energy-harvestable antibiofilm surfaces.

*Corresponding Authors: Geelsu Hwang, geelsuh@upenn.edu; Albert Kim, albertkim@temple.edu.

Associated Content

Equation sets to calculate Owens-Wendt surface energy, zeta potential, and mechanical properties; Schematic for the fabrication of BTO discs; Homogeneity of BTO in the nanocomposites; Antibiofilm activity of BTO discs of varying size; Bactericidal test for BTO discs; Surface roughness of BTO discs of varying size; Total interaction energy profiles between *S. mutans* and BTO discs of varying wt% and size; X-ray diffraction pattern of poled and unpoled BTO discs; Representative confocal images of *S. mutans* biofilms on top and bottom surfaces at 18 h for control, unpoled and poled BTO-nanocomposite discs; Flexural strength and modulus of BTO discs; Mean time to failure and leaching data for BTO discs; Surface energy parameters for Owens-Wendt method; Contact angles, zeta potentials and surface energy for BTO discs and *S. mutans*; Surface energy parameters used for xDLVO modeling; Surface parameters for top and bottom surfaces of unpoled and poled BTO discs; Leaching data for BTO discs.

Keywords

Barium titanate; piezoelectric nanoparticle; infection-resistant biomaterial; *Streptococcus mutans* ; energy-harvestable antibiofilm surface

Introduction

Medical/dental implants and devices have been widely used for the treatment of various diseases as well as in the prosthetic substitution of tissues and organs, including dental, orthopedic, and nasal implants.[1-3] However, the sharp increase in using these implants and devices has led to the development of a new class of microbially-induced infectious diseases due to the rapid bacterial accumulation on material surfaces.[4] When bacteria adhere to surfaces, they often aggregate and form microcolonies while producing extracellular polymeric substances (EPS).[5] Such EPS promotes cell adhesion and cohesion, resulting in a highly structured and adherent biofilm. Notably, once biofilms are established, either killing embedded bacteria or mechanically removing biofilms from surfaces is extraordinarily onerous. Thus, it is imperative to interrupt the bacterial surface sensing mechanism and their initial binding process to surfaces to reduce the prevalence of microbially-induced medical device infections.

Although a range of biomaterials has been fabricated for human use, biofilm-associated infection on medical devices is still an unresolved problem in modern healthcare. An infection resulting from the breaching of soft tissue at the interface with the medical device or implant presents a major hurdle that substantially undermines the clinical applicability and advancement of biomaterial systems.[6, 7] Indeed, 60-70% of all healthcare-associated infections are attributed to implantable medical devices according to the Center for Disease Control.[8] Since these biomaterial-associated infections often involve discomfort, painful and costly surgical intervention,[9] and may even result in life-threatening conditions,[10] the development of infection-resistant biomaterials is crucial to confront pervasive microbial infectious diseases.

Barium titanate ($BaTiO_3$; BTO) is a dielectric material that exhibits piezoelectricity and ferroelectricity. Traditionally, BTO-based devices have been utilized in products such as capacitors,[11] field-effect transistors,[12] and electromechanical devices.[13] Given their attractive piezoelectric properties, BTO-based systems have also found use in biological applications including intravascular ultrasonic transducers for biomedical imaging applications,[14] biocompatible nanogenerators for application as *in vivo* power sources,[15] biocompatible composites for use in bone regeneration,[16] and scaffolds to support cellular survival and proliferation for potential use in personalized bone implants.[17] There have also been attempts to utilize BTO-based systems in antibacterial or oral application. For example, the bactericidal activity of BTO as free nanoparticles in high concentration in solution has been tested.[18, 19] Recently, BTO-embedded surface was tested against *Escherichia coli* using reactive oxygen species (ROS) generated by ferroelectric and photocatalytic routes.[20, 21] Additionally, tooth whitening via piezocatalysis has been reported using poled BTO nanoparticles in liquid form.[22] We also recently utilized a BTO-embedded dental

crown composite to develop a self-powered smart dental implant system for *in situ* photo-biomodulation therapy by utilizing its piezoelectrical property.[23] Yet, despite its versatility, the feasibility of bimodal BTO-embedded biomaterials as anti-adhesive implantable medical devices and sustainable power sources has not been explored in a biological setting with cytotoxicity tests.

Here, we present the first demonstration of bimodal BTO in a bound state, i.e., embedded in a UV-curable polymeric composite (Figure 1) with potent antibiofilm and energy-harvestable functions. Negatively charged BTO-nanocomposites exhibited significant anti-adhesion effects against a model oral biofilm-forming pathogen (*Streptococcus mutans)* while retaining sufficient levels of piezoelectric behavior and mechanical properties for potential clinical uses. Particularly, we observed >10-fold reduction in biofilm colony forming units (CFUs) *in vitro* from 30% BTO-nanocomposites with no bactericidal activity. To reveal the underlying mechanism for this anti-adhesion effect, we provided surface roughness data and interaction energy profiles between BTO-nanocomposites and *S. mutans* using the extended-Derjaguin, Landau, Verwey, and Overbeek (xDLVO) theory corroborated by binding force data using atomic force microscopy (AFM). Interestingly, poling process charged BTO-nanocomposites oppositely on each side, which may enhance tissue integration on a positively charged surface while maintaining significant antibacterial adhesion properties on a negatively charged surface. Lastly, to demonstrate biocompatibility, we evaluated the cytotoxicity of our BTO-nanocomposites towards human gingival fibroblasts and keratinocytes (HGFs and HGKs). Overall, we present stable, non-toxic, self-powering BTO-nanocomposites that have broad-scale potential to be used in biological settings.

Experimental Section

Fabrication of BTO-nanocomposites

The schematic for the fabrication of BTO-embedded discs is shown in Figure S1. We fabricated BTO-nanocomposites equivalent in size to hydroxyapatite discs (commonly used in bacterial studies).[24, 25] Hydroxyapatite discs (12 mm diameter and 1.3 mm thick; Clarkson Chromatography Products Inc., South Williamsport, PA, USA) were placed in standard 50 mm Petri dishes (Corning Inc., Corning, NY, USA). 10:1 wt% of polymer:cross-linker was used to prepare polydimethylsiloxane (PDMS) molds (Sylgard® 184, Dow Silicones Corporation, Midland, MI, USA). Uncured PDMS was poured over the hydroxyapatite discs in Petri dishes. The setup was degassed and allowed to cure at 80°C for 2 hours using a vacuum oven (Across International, Livingston, NJ, USA). PDMS molds were extracted from the Petri dishes after curing. For discs with 400 nm BTO, the nanopowder (US Research Nanomaterials Inc., Houston, Tx, USA) and clear resin (FormLabs, Somerville, MA, USA) were mixed to prepare 0 (control), 10, 20, and 30 wt% BTO-resin mixtures. Additionally, 30 wt% BTO discs were also prepared using 50, 200, and 500 nm BTO nanopowder for size-dependence studies. The mixtures were thoroughly stirred overnight on a roller mixer (LC-3DMixer, 3D Systems, Rock Hill, SC, USA). After overnight stirring, mixtures were degassed and poured into the PDMS molds. To obtain a uniform surface, a piece of UV transparency film (Apollo, ACCO Brands, Lake Zurich, IL,

USA) was gently placed onto uncured BTO-resin mixtures while releasing air bubbles out of the mold. Samples were cured under UV (405 nm, SunRay 400, Uvitron International, West Springfield, MA, USA) for 5 minutes. The transparency films were then removed, and the discs were cured under UV for an additional 25 minutes. Cured discs were removed from the PDMS molds and washed with ethanol. To dislodge any loose BTO from the disc surfaces, the discs were sonicated (3X for 10 minutes each) in Milli-Q water (Millipore-Sigma, Burlington, MA, USA). The discs were then autoclaved (121°C and 15 psi) in custom-made disc holders[25-27] and stored for use in experiments. To assure the homogeneity of BTO in the composite, the highest concentration of BTO-nanocomposites (30% BTO-nanocomposites) was subjected to Scanning Electron Microscopy (SEM) (Quanta FEG 250, FEI, Hillsboro, OR, USA) at an operating voltage of 20 kV and particle distribution analysis using ImageJ with nearest neighbor distance (NND) plugin. A representative SEM image of 30% BTO-nanocomposites depicts BTO nanoparticles that are well distributed across the disc (average distance between particles was 1.88 μm (± 0.55); Figure S2).

Strain and culture conditions

S. mutans UA159, a cariogenic oral pathogen and well-characterized EPS producer, was used for the biofilm experiments. Stocks were stored at −80 °C in tryptic soy broth containing 50% glycerol. Strains were grown to mid-exponential phase in ultrafiltered (10 kDa molecular-mass cutoff; Millipore, Billerica, MA, USA) tryptone-yeast extract broth (UFTYE; pH 7.0) containing 1% glucose. Cells were harvested by centrifugation (5500g, 10 min, 4 °C).

In vitro biofilm model

S. mutans UA159 was transferred from stock culture to the culture medium (UFTYE containing 1% glucose) and incubated overnight at 37°C and 5% CO_2. From this culture, bacteria were transferred onto a fresh culture medium and incubated at 37 °C and 5% CO_2 to mid-exponential phase (optical density of 1.0 at 600 nm). Biofilms were grown on saliva-coated discs (control and BTO) that were vertically suspended in 24-well plates using a custom-made disc holder.[25-27] Each well was inoculated with ~ 2×10^6 CFU/mL of *S. mutans* in UFTYE containing 1% sucrose and incubated at 37°C and 5% CO_2 for 18 hours. At the end of the experimental period, biofilms were removed and homogenized by sonication, and the number of viable cells (CFU/mL) was determined on blood agar plates (BD BBL™ Prepared Plated Media: Trypticase™ Soy Agar (TSA II™) with Sheep Blood, Thermo Fisher Scientific, Waltham, MA, USA).[25, 27] Three experiments were conducted in duplicate.

Biofilm analysis by confocal microscopy

Biofilms were examined using confocal laser scanning microscopy (CLSM) combined with quantitative computational analysis. Briefly, *S. mutans* cells were stained with 2.5 μM SYTO 9 green-fluorescent nucleic acid stain (485/498 nm; Molecular Probes Inc., Eugene, OR, USA) and EPS glucans were labeled with 1 μM Alexa Fluor 647-dextran conjugate (647/668 nm; Molecular Probes Inc.) as detailed previously.[28] The confocal images were obtained using an upright single-photon confocal microscope (LSM800, Zeiss, Jena, Germany) with a 20X (numerical aperture, 1.0) water objective. Each component was

illuminated to minimize crosstalk as follows: SYTO 9 (*S. mutans*) was excited using 488 nm and was collected by a 480/40 nm emission filter, and Alexa Fluor 647 (EPS) was excited using 640 nm and collected by a 670/40 nm emission filter. Biofilms were imaged at 18 h after seeding microorganisms on the discs. Image stacks for each channel were converted to 8-bit ome.tiff files and the COMSTAT plugin of ImageJ[29] was used to generate values for biovolume ($\mu m^3/\mu m^2$). Biovolumes of *S. mutans* and EPS glucans were quantified using COMSTAT2 as detailed elsewhere.[27, 30-32] Three independent experiments were conducted in duplicate for confocal imaging. Biovolumes from each channel were quantified for 6 representative images from each condition.

Assessing bactericidal activity

Bactericidal activity was assessed as detailed elsewhere.[33] Briefly, *S. mutans* UA159 was transferred from stock culture to the culture medium (UFTYE) containing 1% glucose and incubated overnight at 37 °C and 5% CO_2. From this culture, bacteria were transferred onto a fresh culture medium and incubated at 37 °C and 5% CO_2 to an optical density of 1.0 at 600 nm. 50 μl of 2 x 10^5 *S. mutans* was inoculated on blood agar plates, followed by covering spots with control or BTO discs. After incubation for 24 h at 37 °C and 5% CO_2, the viability of *S. mutans* was determined. Three experiments were conducted in duplicate.

Measurement of surface roughness

Sample topography was imaged to measure the roughness of the BTO-nanocomposite discs by a non-destructive confocal contrasting method using Zeiss LSM800 with a C Epiplan-Apochromat 50X (numerical aperture, 0.95) non-immersion objective in air. The images were processed using ConfoMap (Zeiss) to create 3D topographical renders. Arithmetical mean height (S_a) was measured using ISO 25178[34] with a 12.8 μm x 12.8 μm scan area per data point. S_a values were measured for 10 randomly selected areas across each sample. Experiments were conducted in triplicate.

Measurement of contact angles and surface energy

Contact angles for 3 μL drops of Milli-Q water (MilliporeSigma), formamide (Sigma-Aldrich, St. Louis, MO, USA), and diiodomethane (MilliporeSigma) were measured using the sessile drop method[35, 36] on a contact angle goniometer (Ossila Ltd., Sheffield, UK). For BTO-nanocomposites, drops were allowed to stabilize on the surface for 90 s before measurement. For bacterial lawns, a protocol was developed as an adaptation of previous studies.[37, 38] Briefly, 3 starter cultures (grown for 16 h overnight) were used to form bacterial lawns on 0.22 μm PES (polyethersulfone) membranes (Millipore-Sigma). Samples were air-dried for 60 min to reach the plateau contact angle. Drops were allowed to stabilize for 4 s before measurement. Three independent runs were conducted with 10 drops per sample. Surface energy values for BTO-nanocomposites and lawns of *S. mutans* were estimated by the Owens-Wendt method[35, 39] using three test liquids—water, formamide, and diiodomethane. Surface free energy parameters[40] (Table S1) and average contact angles were used to calculate polar and dispersive surface energies from Equation S1.

Measurement of interaction energies between *S. mutans* and BTO-nanocomposite discs

The xDLVO theory was used to measure the interaction energy between *S. mutans* and BTO-nanocomposite discs assuming the bacteria as spheres and the BTO-nanocomposite discs as semi-infinite plates. The protocol followed was adapted from previous studies.[37, 38] Values for components of the interaction energy were calculated using Equation Set S2. Zeta potential values for *S. mutans* were measured in Milli-Q water using a Delsa Nano C particle analyzer (Beckman Coulter, Indianapolis, IN, USA) at the optimal intensity in photon counts/s (16 h overnight starter cultures and dilutions were used to maintain samples in the optimal intensity range). Surface potential values for BTO-nanocomposite discs were measured using AFM in Kelvin Probe Force Microscopy mode (KPFM on an MFP-3D AFM, Asylum Research, Oxford Instruments, Goleta, CA, USA) in Milli-Q water as detailed previously[41] using AC240TM cantilevers (Si with Ti/Pt tip coating; ElectriLever, Asylum Research). Zeta potential values for the BTO-nanocomposite discs were estimated using the surface potential values in Equation S3.[42]

Measurement of binding forces between *S. mutans* and BTO-nanocomposite discs

A previously established protocol for single-cell AFM[27] (sc-AFM) was adapted for use in this study. Briefly, to functionalize the AFM probe with *S. mutans*, tipless cantilevers (PNP-TR-TL-50, NanoWorld, Watsonville, CA, USA) were used. The probes were immersed in poly L-Lysine (pLL) solution (0.1%, Sigma-Aldrich, St. Louis, MO, USA) for 2 min to facilitate bacterial binding. pLL-coated cantilevers were then incubated with washed bacterial cells for another 2 min. After binding, the functionalized probes were washed using phosphate-buffered saline (PBS, HyClone Laboratories Inc., Logan, UT, USA). 10 x 10 adhesion force maps were obtained for 4 random spots per disc with 3 independent runs from distinct culture preparations. Overall, 1200 force-distance curves per condition were analyzed using AtomicJ.[43]

Poling of BTO-nanocomposite discs and assessing antibiofilm activity

To further elucidate the anti-adhesive mechanism of BTO-nanocomposite discs in relation to their piezoelectric nature, 30% BTO-nanocomposites were subjected to poling process. The discs were loaded to our custom-made poling stage, which can hold the discs between a copper bottom plate and a spring-loaded needle electrode from the top. The poling stage with discs was submerged in a silicone oil bath while heated near Curie temperature of BTO (> 80 °C). This is to decompose electric dipoles so that an externally applied strong electric field can align them. Using the poling stage and a high voltage source (230-30R, Spellman, Hauppauge, NY, USA), a uniform electric field of 1kV/mm was applied across the discs. The total poling time was 2 hours. Discs in custom-made holders[25-27] were placed in 1% bleach for 30 minutes followed by sterilization under UV for 30 minutes and stored for use in experiments.

The crystal structure of BTO discs was determined using an X-ray diffractometer (XRD; D8 advance powder XRD, Bruker, Billerica, MA, USA) with Cu-Kα radiation (λ = 1.5418 Å, 40 kV, 40 mA) operating in the reflection mode. The spectrum was obtained for the 2θ range between 20° and 80° with 0.0205° increment and 2 s per step.

For estimation of CFU/mL on top and bottom surfaces of the discs, *S. mutans* biofilms were grown on saliva-coated discs (control, unpoled, and poled) as described in the '*In vitro* biofilm model' section. At the end of the experimental period, the biofilm from each surface was scraped off with a sterile spatula into separate tubes instead of sonicating the entire disc. Further steps remained unchanged.

Measurement of piezoelectric properties

The piezoelectric output of the BTO-nanocomposite discs was characterized by measuring voltage output under mechanical stimulation. BTO-nanocomposite discs with 400 nm BTO nanopowder at 0, 10, 20, and 30 wt% were used. To provide electrical connections, small areas on both sides of the discs were deposited with nickel (M.G. Chemicals, Burlington, ON, Canada) and copper wires were attached using silver epoxy (8331, M.G. Chemicals). The discs were then placed on a custom-made mechanical vibration table, which could provide up to 1 mm of displacements at 500 kHz. Voltages were measured using an oscilloscope (MSOX3024T, Keysight Technologies, Santa Rosa, CA, USA). Voltage measurements were repeated 5 times for 4 BTO discs per concentration.

Measurement of mechanical properties and stability

Three-point flexural strength tests were performed by following ISO 4049 (Dentistry – Polymer-based restorative materials) guidelines.[44] Test specimens were prepared using the previously described fabrication procedure at dimensions of 2 mm × 2 mm × 25 mm. A total of 48 test specimens were prepared (12 each for 0, 10, 20, and 30 wt%). Load and deformation were measured using an electromechanical testing machine (311R, TestResources Inc., Shakopee, MN, USA) and a three-point flexural test fixture. Flexural strength (FS) and flexural modulus (FM) values were then calculated using Equation set S4. The long-term stability of BTO discs was also assessed. We employed the Arrhenius model and experimentally measured the mean-time-to-failure (MTTF) in an accelerated condition (i.e., high temperature), which is defined by Equation S5. To obtain the activation energy, the daily weight of BTO-nanocomposite discs was monitored for 14 days while the discs were kept in two different temperatures in aqueous environments (6 each at 65 °C and 80 °C in DI water). Each sample's weight was measured (Aczet Inc., Piscataway, NJ, USA) after taking the sample out of DI water and removing moisture. The 14-day weight loss was then modeled based on an exponential decay (Equation S6).[45] Using the weight loss model, we estimated the MTTF with failure corresponding to the BTO-nanocomposite discs reaching 90% of its initial state. The activation energies were obtained by solving the Arrhenius model (Equation S6) with experimentally measured MTTFs for 14 days at 65 °C and 80 °C. Lastly, the lifespan at normal operating temperature (37 °C) was estimated by calculating the acceleration factor (AF) between each temperature (37 °C vs. 65 °C and 37 °C vs. 80 °C) using Equation S7.

Measuring cytotoxicity towards HGFs and HGKs

Extract-based cytotoxicity screening assays were performed on HGFs (kindly provided by the laboratory of Dr. Jonathan Korostoff, School of Dental Medicine, University of Pennsylvania) and HGKs (kindly provided by the laboratory of Dr. Dana T. Graves, School of Dental Medicine, University of Pennsylvania) following ISO 10993-5 guidelines.[34] Cells

were maintained in their respective culture media (HGFs: Fibroblast Basal Medium (ATCC, Manassas, VA, USA) supplemented with Fibroblast growth kit (ATCC, PCS-201-041) and 1% v/v Anti-Anti (Gibco, Gaithersburg, MD, USA); HGKs: Keratinocyte Basal Medium (KBM-Gold, Lonza Group AG, Basel, Switzerland) supplemented with KGM-2 SingleQuots kit (Lonza) and incubated at 37 °C in a humidified atmosphere of 5% CO_2 until confluence. BTO-nanocomposite and control discs were placed in serum-free media for the respective cells and used for extract testing following ISO guidelines for surface area/volume ($3cm^2$/mL). For cytotoxicity screening, cells were seeded in 100 μL of culture media (5000 cells/well in 96-well plates). The next day, the media was replaced with spent media from the extracts for the treatment time (1 h and 24 h). After treatment, well volumes were replaced with fresh serum-free media and left for a total of 24 h. 0.5% phenol treatment for 1 h was used as a cytotoxic control. The next day, 10 μL of MTT reagent (Sigma-Aldrich, St. Louis, MO, USA) was added to 90 μL of fresh serum-free media. Samples were left for 5 hours. Well volumes were then replaced with DMSO (Sigma-Aldrich, St. Louis, MO, USA). Absorbance values were read at 570 nm using a SpectraMax M2 (Molecular Devices, Sunnyvale, CA, USA). Percentage cell viability was calculated from the absorbance readings. Three independent experiments were conducted in triplicate.

Statistical analyses

All statistical analyses for biochemical, microbiological, biovolume, and topographical data were carried out using GraphPad Prism 9 via i) analysis of variance (ANOVA), followed by Dunnett's test for post-hoc analysis or ii) Student's t-test where appropriate. The level of significance was set at 5%.

Results

Antibiofilm activity of BTO-nanocomposite discs

Given the limited evidence of the biological usefulness of BTO nanoparticles in terms of antibiofilm and antibacterial behavior, we tested our BTO-nanocomposite discs to assess their susceptibility to bacterial binding. The piezoelectric properties of BTO nanosystems are normally dictated by their crystal size;[46, 47] particles with a size greater than 100 nm typically form tetragonal crystal systems and display sufficient piezoelectricity.[48] Thus, with the consideration of the broader application for biomedical implant devices, we chose 400 nm BTO nanoparticles for use in BTO-nanocomposite disc fabrication and investigated their biological actions (see Experimental Section and Figure S1 for details). Then, we measured the antibiofilm activity of 400 nm BTO-nanocomposite discs with varying BTO wt% using *S. mutans* UA159 in an established *in vitro* model.[25, 27] Interestingly, the discs displayed a dose-dependent reduction in CFU/mL (Figure 2A) with increasing wt% of BTO; a similar amount of bacteria bound to 10 wt% BTO-nanocomposite discs (vs. control disc with no BTO) while the amount started reducing when BTO content was higher than 20 wt%. At the highest wt% (30%), we measured a significant 10-fold reduction in CFU/mL when compared to the control discs. Additionally, we tested the antibiofilm activity of 30 wt% BTO-nanocomposite discs made from varying sizes (50-500 nm). Encouragingly, the antibiofilm nature of the BTO-nanocomposite discs persisted (~10-fold reduction) with no significant differences in CFU/mL between discs made from varying sizes of BTO (Figure

S3). This indicates that the wt% of BTO added to the discs played a dominant role in the drop in biofilm formation.

To further understand the differences in biofilm properties on the discs, we investigated the microbial growth and tertiary structures of the biofilms using confocal microscopy. Representative confocal images to visualize the drastic reduction in CFU/mL at 18 h are shown in Figure 2B. As shown, there were significantly fewer microcolonies of *S. mutans* (labeled as green) on discs with 30 wt% BTO in comparison to control discs with no BTO. This reduction was also observed in the amount of EPS (labeled as red) on the disc surfaces. Overall, the biofilms on BTO-nanocomposites were thinner than those observed on the control discs. Interestingly, the 30 wt% BTO-nanocomposite discs had bacterial microcolonies that were sparse and not well connected. To quantify the changes in confocal imaging, we determined the biovolume of *S. mutans* and EPS (Figures 2C-E). Image quantification analysis coincided with our bacterial population data on 30 wt% BTO-nanocomposite discs (CFU/mL) in comparison to control discs, showing ~10-fold reduction in *S. mutans* biovolume (Figure 2C) accompanying a ~3.5-fold reduction in biovolume of produced EPS (Figure 2D). Overall, there was a combined ~6-fold reduction in total biovolume of the biofilm on BTO-nanocomposite discs (vs. control; Figure 2E).

Then, we performed further experiments to investigate the underlying mechanism of biofilm prevention activity of BTO-nanocomposite discs by determining whether the antibiofilm nature of BTO-nanocomposite discs was due to bacterial killing or repelling bacterial adhesion. First, we conducted 24 h contact tests of BTO-nanocomposite discs with colonies of *S. mutans* growing on blood agar plates to assess bactericidal activity. Intriguingly, both BTO-nanocomposite and control discs had no bactericidal activity; *S. mutans* grew regardless of the BTO content (Figure S4). The results strongly postulated that the drop in biofilm formation on the BTO-nanocomposite discs could be primarily due to an anti-adhesion effect. Thus, to validate our hypothesis of an anti-adhesion effect preventing biofilm formation and understand the mechanism of action of such bacterial repelling behavior, we comprehensively analyzed the surface properties of the control and BTO-nanocomposite discs.

Surface Roughness of BTO-nanocomposite discs

Among various surface properties affecting bacterial adhesion, surface roughness is one of the critical factors.[5] Therefore, we performed an ISO 25178[49] test in non-contact mode using optical sectioning on a confocal microscope. As expected, embedding BTO nanoparticles into resin mixtures led to a small increase in surface roughness. Arithmetical mean height values (S_a) rose in a dose-dependent manner with increasing wt% of BTO (Figure 3A). Representative images for discs with increasing wt% of BTO indicated a gradual increase in roughness (Figure 3B). Furthermore, we conducted the same topographical assessment of 30 wt% BTO-nanocomposite discs with varying sizes (50-500 nm). The S_a values for discs with 200, 400, 500 nm BTO nanoparticles showed similar surface roughness values, while those for discs with 50 nm BTO nanoparticles presented significantly lower surface roughness values similar to control discs (Figure S5). Since *S. mutans* binding was inversely proportional to the BTO wt% (Figure 2) and its pattern to 30%

wt BTO discs was similar regardless of surface roughness values (Figure S3 and S5), the data confirmed that surface roughness did not play a large role in the antibiofilm nature of BTO-nanocomposite discs.

Interaction energy between *S. mutans* and BTO-nanocomposite discs

To delve deeper into investigating the mechanism behind the antibiofilm activity of BTO-nanocomposite discs, we estimated their surface energies. Given that the Owens-Wendt method (Equation S1) is best suited for polymeric surfaces containing methacrylates (the base material of our discs),[50, 51] we utilized this method to determine if differences in polar and dispersive components of surface energy could explain the anti-adhesion effect. First, we determined the contact angles of control and BTO-nanocomposite discs with previously established parameters[40] for 3 reference liquids – water, formamide, and diiodomethane (Table S1) to estimate the polar and dispersive components of the discs. Results indicated an increase in polar surface energy with increasing wt% of BTO while the overall surface energy did not change significantly. We also observed a similar trend for BTO-nanocomposite discs with varying sizes of BTO (50–500 nm). Additionally, we used the same method to estimate the surface energy for lawns of *S. mutans*. These results are compiled in Table S2. Our results for the contact angles and surface energy of *S. mutans* were in close agreement with previous studies.[52]

Since the data indicated that BTO nanoparticles altered the polar interaction properties of the disc surfaces, we modeled the interaction energy between *S. mutans* and discs using xDLVO theory to further explain *S. mutans*' binding behavior on control and BTO-nanocomposite discs. The xDLVO theory provides an estimate for the total interaction energy between two surfaces by accounting for Lifshitz–van der Waals (LW) interactions, electrostatic interactions (EL), and the acid-base interactions (AB) that the two surfaces encounter in their environment. It has been extensively used to model the interactions between bacteria and solid surfaces.[37, 38, 52, 53] Here, we used it to model the interaction between *S. mutans* (assumed to be a sphere) and 30 wt% BTO-nanocomposite discs (vs. control discs; assumed to be semi-infinite plates) using Equation S2 and S3. Briefly, contact angles for the 3 test liquids (same as the Owens-Wendt method above) and zeta potentials of the discs and *S. mutans* (Table S2) were used to calculate the LW, EL and AB interaction energies (ΔG^{LW}, ΔG^{EL} and ΔG^{AB}, respectively) as a function of the separation distance between *S. mutans* and the discs (using parameters in Table S3).

The resultant interaction energies for 30 wt% BTO-nanocomposite (400 nm) and control discs are shown in Figure 4A. Clearly, the ΔG^{AB} interactions dominated the types of interactions for both disc surfaces. The ΔG^{LW+EL} (classical DLVO theory) interaction energies are shown separately in Figure 3B, which presents an unfavorable energy barrier for *S. mutans*-BTO-nanocomposites interaction compared to the profile for *S. mutans*-control disc. This indicated that the BTO-nanocomposite discs with a higher negative surface charge density (vs. control discs; from zeta potentials in Table S2) prevented the adhesion of *S. mutans* (also negatively charged). This effect was amplified with the ΔG^{AB} interactions added in (to complete the xDLVO components – Figure 4C). At separation distances under 5 nm, the total interaction energies profiles separate out in opposite directions, resulting in

an unfavorable barrier for *S. mutans*-BTO-nanocomposites interactions while a relatively favorable profile for *S. mutans*-control disc interactions. The inset in Figure 4C depicts a magnified view of the interaction energy profiles with opposing tendencies. We also calculated the profiles for 10 and 20 wt% 400 nm BTO-nanocomposite discs (Figure S6A). The interaction energy profiles clearly support the trend in antibiofilm activity varying with BTO wt% (Figure 2) with 30 wt% discs displaying the most unfavorable profile for adhesion, followed by 20 wt%, 10 wt%, and control discs. As with our previous results, we tested this model with varying sizes of BTO (50–500 nm) and found that the interaction energy profiles for *S. mutans*-BTO-nanocomposites interactions were always unfavorable and opposed to *S. mutans*-control disc interactions regardless of the size of the BTO nanoparticles used to fabricate the discs (Figure S6B).

Our xDLVO modeling data in Figure 4 provided strong anti-adhesion evidence as an explanation for the mechanism of the antibiofilm activity seen in Figure 2. The data also suggest that the antibiofilm activity of the BTO discs in comparison to control discs is likely due to an intrinsic anti-adhesion effect that presents an unfavorable binding environment for *S. mutans*.

Binding forces between *S. mutans* and BTO-nanocomposite discs

To corroborate the xDLVO theory and the proposed anti-adhesion mechanism for antibiofilm activity, we measured *S. mutans* - disc interactions (i.e., direct cell-to-surface binding force) via biophysical measurements using sc-AFM (see Experimental Section for details). We observed clear differences in binding force patterns between *S. mutans* - control and *S. mutans* - BTO-nanocomposite discs. The binding force distribution for *S. mutans* - control discs was broad with ~50% of the adhesion force values lying in the 3 most populated bands (between 1-1.6 nN). The highest force value for this distribution was 2.51 nN. The binding force distribution for *S. mutans* - BTO-nanocomposite discs was narrow with ~70% of the adhesion force values lying in the 3 most populated bands (between 0.4-1 nN). The highest force value for this distribution was 1.09 nN. Overall, the average binding forces for *S. mutans* - BTO-nanocomposite discs were ~2.25-fold lower (~0.4 nN compared to ~0.9 nN) than those for *S. mutans*-control discs (Figure 5A). Representative force curves for these interactions are shown in Figure 5B. These representative curves also highlight a longer and “stickier” rupture of the interaction between *S. mutans* - control rather than *S. mutans* - BTO-nanocomposite discs. Overall, this provides strong evidence to support both the findings of actual *S. mutans* binding patterns to discs and their modeled interaction energies (Figure 2 and 4).

Effect of poling process on antibiofilm activity of BTO-nanocomposite discs

Next, we further elucidated the anti-adhesive mechanism of BTO-nanocomposite discs in relation to their piezoelectric nature. We evaluated the surface roughness, contact angles, Owens-Wendt surface energy, and zeta potentials for both surfaces of poled and unpoled BTO-nanocomposite discs (Table S4).

First, we verified the poling by obtaining the crystal structures and orientation using XRD on the fabricated 30% BTO-nanocomposites before and after poling (Figure S7).

The diffraction peak positions were in good agreement with previous literature.[54, 55] The tetragonal phase of $BaTiO_3$ was confirmed by the peak splitting at 2θ near 22° and 45°. Furthermore, the enhancement of peak ratios of (001)/(100) and (002)/(200) was observed after poling, indicating the piezoelectric domains are aligned along the poling direction of (001).

While the surface roughness, contact angle, and surface energy data did not vary significantly for the top and bottom surfaces of poled and unpoled discs, the poling process altered the zeta potential of one surface of poled discs resulting in positive values (Table S4). Then, we determined the bacterial binding on each surface of control, poled, and unpoled discs with 30 wt% BTO of 400 nm individually (Figure 6). For convenience, we named a more negatively charged surface as the top. Interestingly, the positively charged surface (bottom) of poled discs favored bacterial binding and did not show significant antibiofilm activity (vs. both surfaces of control discs). On the other hand, the negatively charged side (top) of poled discs demonstrated a slight improvement in the reduction of bound bacteria (vs. unpoled BTO-nanocomposites). This directly supports our proposed mechanism of the antibiofilm activity via repulsive interaction between bacteria and surfaces depending on the physicochemical properties of the surface. Representative confocal images depicting this distinction in bacterial binding behavior on top and bottom surfaces of the discs are shown in Figure S8.

Piezoelectric and mechanical properties of BTO-nanocomposite discs

To be a useful emerging biomaterial, BTO-nanocomposite discs also need to retain their intrinsic piezoelectric properties. Thus, we confirmed that the composites maintained their piezoelectric behavior and mechanical stability, in addition to their antibiofilm activity shown above. We evaluated the piezoelectric properties of BTO-nanocomposite discs (with BTO size of 400 nm) by measuring voltage outputs under mechanical vibration. The output voltages showed a promising BTO concentration-dependency; voltage output increased proportionally and substantially to the BTO concentration (Figure 7A and B). 30 wt% BTO-nanocomposite discs demonstrated ~35-fold improvement in output voltage compared to control discs (~32-fold and ~26-fold improvement over control discs for 20 wt% and 10 wt% BTO-nanocomposite discs, respectively).

Additionally, we tested the mechanical strength (FS and FM) of the BTO-nanocomposite discs to evaluate the impact of the addition of BTO nanoparticles. We observed a small reduction in FS of up to 24.87 MPa for the 30 wt% BTO-nanocomposite discs in comparison to control discs. Our results were comparable to previous studies involving dental applications.[23, 56, 57] The FM values fluctuated with BTO concentration with no clear, significant differences (Figure S9). These results were comparable with our recent work on a Smart Dental Implant[23] indicating that our discs were suitable for potential use in biological settings.

Long-term stability is another important parameter for determining the durability of biomaterials in a biological environment. Therefore, we tested the leaching of BTO nanoparticles from the discs to their surroundings. We also used an industrial standard, accelerated life testing, to estimate the MTTF of the discs (Table S5 and Figure S10).

The long-term stability of discs was modeled by assessing the daily weight lost over a 14-day period and estimating the MTTF at 37 °C, 65 °C, and 80 °C by measuring the AF. Excitingly, we observed negligible loss of the disc over a 14-day period under 37 °C, exhibiting lifetime durability. Indeed, MTTF of 30% wt BTO disc at 37 °C was estimated to be approximately 27.5 years. Even under harsh conditions (clinically irrelevant) such as at 65 °C and 80 °C, the discs only lost ~1 mg (<0.4%) over 14 days and the estimated MTTFs were close to 1,000 days and a year, respectively (Figure S10A and B). The data indicate that our BTO-nanocomposite discs exhibit reliable durability under clinically relevant conditions against external forces and temperatures without compromising their antibiofilm and piezoelectrical properties.

Cytotoxicity towards human gingival fibroblasts and keratinocytes

Previous biological studies involving free BTO nanoparticles did not assess the cytotoxicity of BTO.[18, 19] In this study, we studied the antibiofilm activity of BTO-nanocomposite discs against a model oral pathogen, *S. mutans*. To be useful in the oral environment and as an extension to our recent work on BTO-dental crown composites,[23] the cytotoxicity of BTO-nanocomposite discs needs to be assessed in an appropriate cellular environment. Thus, we followed ISO 10993-5[34] guidelines to perform an extract cytotoxicity test on 30 wt% BTO discs (with BTO size of 400 nm) and control discs against human gingival cells (HGFs and HGKs). The data from MTT assays performed with spent media (media in contact with samples for 24 h at 37 °C and 5% CO_2) demonstrated no significant drop in cell viability for either cell line (Figure 8A – HGFs and 8B – HGKs) with treatment times of 1 h and 24 h. This result complied with the non-leaching data from Figure S10. On the other hand, cytotoxic controls with 0.5% phenol led to an almost complete loss in cell viability for both cell lines. In summary, all the data strongly suggested that the BTO-nanocomposites can serve as a platform for biomaterials that require microbial infection resistance and electrical power for functionality.

Discussion

Rapid advances in micro and nanotechnology have led to a dramatic upgrade in the usefulness of implantable biomaterials making them increasingly advantageous in disease monitoring, diagnosis, and treatment.[58] Furthermore, recent progress in microelectronics enables communication of implantable devices with external devices worn by the host/user. To reliably fulfill their function over a long-term period, however, such devices require sustained power generation. Yet, these devices are often limited by the size, capacity, and lifespan of their batteries, which require frequent replacement if not rechargeable (rechargeable batteries allow up to 1,000 charge cycles). Concomitantly, these implantable devices should be infection-resistant to avoid severe, painful, and costly surgical replacement due to failure. The most common methods for controlling microbially-induced infections include antimicrobial coatings (e.g., leachable[59] and non-leachable[60]). However, the escalating pervasiveness of antimicrobial resistance hinders these approaches and the management of biomaterial-associated infections.[6] To address both sustained energy production and biomaterial-associated infection, in this study, we aimed to develop an ingenious multi-functional biomaterial platform utilizing BTO as a smart

component, exhibiting excellent piezoelectricity and outstanding bacterial binding repellant properties without relying on an antimicrobial component. Then, we comprehensively analyzed the biological, electrical, and mechanical properties of BTO-nanocomposites to significantly broaden BTO's potential applications for infection-resistant, non-toxic, and energy-harvestable biomaterial platforms.

Our highly reproducible fabrication strategy (Figure S1) was optimized to ensure that the BTO-nanocomposite discs retained potent piezoelectric and mechanical behavior while also serving as candidates to run established *in vitro* oral biofilm assays.[25, 27] By performing proof-of-concept biofilm assays against a model oral pathogen, *S. mutans*, we demonstrated >10-fold reduction in bacterial population bound to BTO-nanocomposite discs (vs. control; Figure 2 and 6). Previous studies with BTO nanoparticles have shown moderate bactericidal activity.[18, 19] However, these results were for free nanoparticles with concentrations as high as 100 μg/mL. Additionally, the size of the BTO nanoparticles (smaller than the diameter of 100 nm) prevented them from demonstrating any piezoelectric behavior in biologically relevant conditions. In this study, we primarily demonstrated the biological usefulness of piezoelectrically-active BTO-nanocomposite discs with a particle size of 400 nm at different wt% (0-30 wt%). Nevertheless, the antibiofilm activity of our BTO-nanocomposite discs persisted regardless of the size of the BTO used (Figure S3). Notably, the BTO-nanocomposite discs were able to reduce the number of bound bacteria to the surface without displaying any bactericidal activity (Figure S4). In comparison to conventional therapies, such non-microbicidal approaches can be extremely beneficial as they may not disrupt normal microflora nor induce the prevalence of drug resistance over time.

Given that the BTO-nanocomposite discs did not depict any bactericidal activity, we surmised that BTO-nanocomposite discs may display an anti-adhesive effect to prevent biofilm formation. To investigate this claim, we first investigated the effect of surface roughness of the discs on *S. mutans* adhesion. Some studies reported that surface roughness increased bacterial adhesion.[61, 62] In our study, we observed that the surface roughness increased with increasing BTO content and size; the mean surface roughness value of 30 wt% BTO-nanocomposite discs was ~4-fold higher than that for control discs, while the overall roughness was indeed under 100 nm for all discs. However, our binding data showed that the magnitude of bacterial binding coincided with BTO content rather than surface roughness (Figure 2 and 3). Although surface roughness can act as a determinant to govern bacterial binding to surfaces, it should not be used as the sole descriptor to explain adhesion on surfaces [63]. Since there are many other factors affecting bacterial adhesion, bacterial binding can be varied to surfaces with the same roughness, depending on other material properties (e.g., charge density, wettability, stiffness, and topography) and bacterial species.[5] Interestingly, Lassila et al. [64] have previously reported that there was no change in the adhesion of *S. mutans* to composite resins and commercial restorative materials of varying roughness values (R_a ranging from 0.3 to 2.3 μm) indicating that the adhesion of *S. mutans* can be dependent on other surface parameters. In particular, the scale of the roughness of the BTO-nanocomposite and control discs tested in our study is consistent with nano-enabled mechanisms where physicochemical forces dominate parameters affecting adhesion.[63]

The zeta potential values of the substrate clearly indicate that BTO-nanocomposite discs had a higher negative surface charge density in comparison to the control discs (Table S2). Additionally, the zeta potential values for *S. mutans* were in agreement with a previous study on various isolates of *S. mutans*[65] depicting low negative values near neutral pH. This helped us elucidate the mechanism of the anti-adhesive action of our BTO-nanocomposites using xDLVO modeling (Figure 4). As expected, the AB interactions dominated the LW+EL component in an aqueous environment.[42] The trend in these profiles did not change with varying the size of BTO (Figure S6) indicating that negatively charged BTO may intrinsically be preventing binding of negatively charged *S. mutans* in an aqueous environment. While the modeled data was strongly suggestive of the anti-adhesive behavior of our BTO-nanocomposite discs, sc-AFM data (Figure 5) experimentally and quantitatively confirmed that the anti-adhesive character of the BTO-nanocomposite discs was a major driving force to inhibit *S. mutans* adhesion. It is worth noting that we observed antibiofilm activity on both poled and unpoled discs with varying degrees of efficacy depending on the attractive/repulsive interactions between specific surfaces of the discs and *S. mutans*. Specifically, the positively charged surface of the poled disc with no significant antiadhesive property (Figure 6) supports our proposed mechanism of the antibiofilm activity via repulsive interaction between bacteria and surfaces. Our BTO-nanocomposites utilize the unique physicochemical surface properties that inhibit bacterial adhesion, while recent studies of BTO-based systems utilize ROS to kill *E. coli*,[20, 21] which could be temporary in the human body (e.g., in the mouth) as the ROS generation is subjected to mechanical stimuli.

The opposite charge of BTO-nanocomposites on each side by poling process may provide additional benefits in biomedical applications. As we observed in this study, a negatively charged surface could inhibit bacterial adhesion to the surface. In contrast, a positively charged surface could facilitate the integration of biomaterial into soft tissues as reported elsewhere.[66-69] Our intended application in the oral cavity involves the negatively charged surface facing outwards (exposed to saliva and bacterial insults) and the positively charged surface facing inwards (towards tissue). This may allow us to synergistically integrate the two functions of our BTO-nanocomposites by placing them accordingly, thereby tackling two major issues in prosthetics- bacterial contamination and tissue integration. It is important to mention that the poling electric field and nanoparticle concentration can dictate the magnitude of surface charge, which should be further explored in future studies.

Notably, our data also demonstrated other important features of multifunctional BTO-nanocomposites that can potentially benefit many implantable devices. For example, the substantial mechanical strength of our BTO-nanocomposite (Figure S9) warrants a wide adoption as simple packaging. As we demonstrated tangible electrical outputs using the piezoelectricity of BTO (Figure 7), it can also be useful for low-power electronics. Furthermore, the long-term stability data (low leaching and MTTF; Table S5 and Figure S10) strongly suggest that our BTO-nanocomposites are less likely affected by the gradual and passive loss of antibiofilm effect, which has been a major drawback of many of the antibiofilm materials. Finally, the confirmed biocompatibility, provided by the absence of cytotoxicity towards HGFs and HGKs (Figure 8), bodes well for translation into biological settings and clinical applications. There has been a report that Ba^{2+} can be leached out

from free-floating BTO surfaces.[70] However, we did not observe significant cytotoxicity to gingival keratinocytes and fibroblasts that can be caused by leaching of BTO from the disc, possibly due to the low surface area of BTO tightly embedded in the nanocomposites. Altogether, the data strongly suggest that our BTO-nanocomposites, with their robustness and ability to resist bacterial contamination, make them attractive candidates for use in the diverse biomedical arena.

Conclusion

In summary, we present the first demonstration of clinically viable infection-resistant energy-harvestable hybrid nanocomposites functionalized with BTO that have adequate mechanical properties and outstanding biocompatibility. The mechanism for this antibiofilm activity was a strong anti-adhesive effect that inhibited *S. mutans* adhesion. Yet, this anti-adhesive property and the underlying mechanisms of BTO-nanocomposites need to be validated against other model pathogens as well as complex multi-species biofilm models to improve the relevance and broaden the scope of its potential uses. Additionally, heterogeneously charged surfaces of poled discs may grant us to address unresolved issues in prosthetics- bacterial contamination and tissue integration. Furthermore, future studies may benefit to further improve the mechanical strength of BTO-nanocomposites by considering other emerging base materials to be compliant with areas facing strenuous cyclic compression loading, such as tibia. This coupled with non-bactericidal activity, stability and non-toxicity suggests that our BTO-nanocomposites can serve as a potent biomaterial platform for developing implantable ambulatory devices in the human body.

Supplementary Material

Refer to Web version on PubMed Central for supplementary material.

Acknowledgements

This work was financially supported by the National Institutes for Dental and Craniofacial Research (NIDCR) grant DE027970 (GH) and the National Science Foundation (NSF) grant 2029077 (AK). It was carried out in part at the Singh Center for Nanotechnology, which is supported by the NSF National Nanotechnology Coordinated Infrastructure Program under grant NNCI-1542153. We would like to thank Drs. Jonathan Korostoff and Dana T. Graves at the School of Dental Medicine, University of Pennsylvania for providing HGF and HGK cells, respectively. We would like to thank Dr. Daeyeon Lee and Mr. Joseph Rosenfeld for the zeta potential measurement of bacteria. We also thank Drs. Seven M. Chemtob and Michael Zdilla at the Department of Chemistry, Temple University for their help with the XRD measurements.

References

1. Lemons JE; Misch-Dietsh F; McCracken MS, Biomaterials for Dental Implants. In Dental implant prosthetics, Elsevier Inc.: 2015; pp 66–94.
2. Griffin M; Premakumar Y; Seifalian A; Szarko M; Butler P, Biomechanical Characterisation of the Human Nasal Cartilages; Implications for Tissue Engineering. Journal of Materials Science: Materials in Medicine 2016, 27 (1), 11. [PubMed: 26676857]
3. Serban MA, Translational Biomaterials—the Journey from the Bench to the Market—Think ‘Product’. Current opinion in biotechnology 2016, 40, 31–34. [PubMed: 26926461]
4. Arciola CR; Campoccia D; Montanaro L, Implant Infections: Adhesion, Biofilm Formation and Immune Evasion. Nature Reviews Microbiology 2018, 16 (7), 397–409. [PubMed: 29720707]

5. Zheng S; Bawazir MM; Dhall A; Kim H-E; Le H; Heo J; Hwang G, Implication of Surface Properties, Bacterial Motility, and Hydrodynamic Conditions on Bacterial Surface Sensing and their Initial Adhesion. Frontiers in Bioengineering and Biotechnology 2021, 9, 82.
6. Bazaka K; Jacob MV; Crawford RJ; Ivanova EP, Efficient Surface Modification of Biomaterial to Prevent Biofilm Formation and the Attachment of Microorganisms. Applied microbiology and biotechnology 2012, 95 (2), 299–311. [PubMed: 22618687]
7. Campoccia D; Montanaro L; Arciola CR, A Review of the Biomaterials Technologies for Infection-resistant Surfaces. Biomaterials 2013, 34 (34), 8533–8554. [PubMed: 23953781]
8. Bryers JD, Medical Biofilms. Biotechnology and bioengineering 2008, 100 (1), 1–18. [PubMed: 18366134]
9. Skrivan J; Drevinek P, A Case Report of a Cochlear Implant Infection–A Reason to Explant the Device? Cochlear implants international 2016, 17 (5), 246–249. [PubMed: 27609547]
10. Bluestone CD, Bacterial Meningitis in Children with Cochlear Implants. The New England journal of medicine 2003, 349 (18), 1772.
11. Donahoe DN; Pecht M; Lloyd IK; Ganesan S, Moisture Induced Degradation of Multilayer Ceramic Capacitors. Microelectronics Reliability 2006, 46 (2-4), 400–408.
12. Cai QJ; Gan Y; Chan-Park MB; Yang HB; Lu ZS; Li CM; Guo J; Dong ZL, Solution-processable Barium Titanate and Strontium Titanate Nanoparticle Dielectrics for Low-voltage Organic Thin-film Transistors. Chemistry of Materials 2009, 21 (14), 3153–3161.
13. Maranganti R; Sharma P, Atomistic Determination of Flexoelectric Properties of Crystalline Dielectrics. Physical Review B 2009, 80 (5), 054109, 1–10.
14. Yan X; Lam KH; Li X; Chen R; Ren W; Ren X; Zhou Q; Shung KK, Correspondence: Lead-free Intravascular Ultrasound Transducer using BZT-50BCT Ceramics. IEEE transactions on ultrasonics, ferroelectrics, and frequency control 2013, 60 (6), 1272–1276.
15. Yuan M; Cheng L; Xu Q; Wu W; Bai S; Gu L; Wang Z; Lu J; Li H; Qin Y, Biocompatible Nanogenerators through High Piezoelectric Coefficient 0.5 Ba (Zr0. 2Ti0. 8) O3-0.5 (Ba0. 7Ca0. 3) TiO3 Nanowires for In-Vivo Applications. Advanced Materials 2014, 26 (44), 7432–7437. [PubMed: 25257019]
16. Tang Y; Wu C; Wu Z; Hu L; Zhang W; Zhao K, Fabrication and In Vitro Biological Properties of Piezoelectric Bioceramics for Bone Regeneration. Scientific reports 2017, 7, 43360. [PubMed: 28240268]
17. Busuioc C; Voicu G; Jinga S-I; Mitran V; Cimpean A, The Influence of Barium Titanate on the Biological Properties of Collagen-hydroxiapatite Composite Scaffolds. Materials Letters 2019, 253, 317–322.
18. Raja S; Bheeman D; Rajamani R; Pattiyappan S; Sugamaran S; Bellan CS, Synthesis, Characterization and Remedial Aspect of BaTiO3 Nanoparticles against Bacteria. Nanomedicine and Nanobiology 2015, 2 (1), 16–20.
19. Shah AA; Khan A; Dwivedi S; Musarrat J; Azam A, Antibacterial and Antibiofilm Activity of Barium Titanate Nanoparticles. Materials Letters 2018, 229, 130–133.
20. Kumar S; Sharma M; Powar S; Kabachkov E; Vaish R, Impact of Remnant Surface Polarization on Photocatalytic and Antibacterial Performance of BaTiO3. Journal of the European Ceramic Society 2019, 39 (9), 2915–2922.
21. Wang R; Zhou T; Liu J; Zhang X; Yang J; Hu W; Liu L, Designing Novel Anti-biofouling Coatings on Titanium based on the Ferroelectric-induced Strategy. Materials & Design 2021, 203, 109584.
22. Wang Y; Wen X; Jia Y; Huang M; Wang F; Zhang X; Bai Y; Yuan G; Wang Y, Piezo-catalysis for Nondestructive Tooth Whitening. Nature communications 2020, 11 (1), 1–11.
23. Park M; Islam S; Kim HE; Korostoff J; Blatz MB; Hwang G; Kim A, Human Oral Motion-Powered Smart Dental Implant (SDI) for In Situ Ambulatory Photo-biomodulation Therapy. Advanced Healthcare Materials 2020, 9 (16), 2000658, 1–10.
24. Takeshita T; Yasui M; Shibata Y; Furuta M; Saeki Y; Eshima N; Yamashita Y, Dental Plaque Development on a Hydroxyapatite Disk in Young Adults Observed by using a Barcoded Pyrosequencing Approach. Scientific reports 2015, 5 (1), 1–9.

25. Kim H-E; Liu Y; Dhall A; Bawazir MM; Koo H; Hwang G, Synergism of Streptococcus mutans and Candida albicans Reinforces Biofilm Maturation and Acidogenicity in Saliva: An In Vitro Study. Frontiers in Cellular and Infection Microbiology 2020, 10, 932.
26. Cocco AR; Cuevas-Suárez CE; Liu Y; Lund RG; Piva E; Hwang G, Anti-biofilm Activity of a Novel Pit and Fissure Self-adhesive Sealant Modified with Metallic Monomers. Biofouling 2020, 36 (3), 245–255. [PubMed: 32326753]
27. Wan S; Tian J; Liu Y; Dhall A; Koo H; Hwang G, Cross-Kingdom Cell-to-Cell Interactions in Cariogenic Biofilm Initiation. Journal of Dental Research 2020, 0022034520950286.
28. Xiao J; Klein MI; Falsetta ML; Lu B; Delahunty CM; Yates III JR; Heydorn A; Koo H, The Exopolysaccharide Matrix Modulates the Interaction between 3D Architecture and Virulence of a Mixed-species Oral Biofilm. PLoS Pathog 2012, 8 (4), e1002623. [PubMed: 22496649]
29. Schindelin J; Arganda-Carreras I; Frise E; Kaynig V; Longair M; Pietzsch T; Preibisch S; Rueden C; Saalfeld S; Schmid B, Fiji: An Open-source Platform for Biological-image Analysis. Nature methods 2012, 9 (7), 676–682. [PubMed: 22743772]
30. Heydorn A; Nielsen AT; Hentzer M; Sternberg C; Givskov M; Ersbøll BK; Molin S, Quantification of Biofilm Structures by the Novel Computer Program COMSTAT. Microbiology 2000, 146 (10), 2395–2407. [PubMed: 11021916]
31. Paula AJ; Hwang G; Koo H, Dynamics of Bacterial Population Growth in Biofilms Resemble Spatial and Structural Aspects of Urbanization. Nature communications 2020, 11 (1), 1–14.
32. Vorregaard M Comstat2-A Modern 3D Image Analysis Environment for Biofilms. Citeseer, 2008.
33. Hwang G; Koltisko B; Jin X; Koo H, Nonleachable Imidazolium-Incorporated Composite for Disruption of Bacterial Clustering, Exopolysaccharide-Matrix Assembly, and Enhanced Biofilm Removal. Acs Applied Materials & Interfaces 2017, 9 (44), 38270–38280. [PubMed: 29020439]
34. ISO 10993-5: 2009 — Biological Evaluation of Medical Devices — Part 5: Tests for In Vitro Cytotoxicity. International Standards Organization: Geneva, Switzerland, 2009.
35. Dhall A; Masiello T; Gattu S; Strohmayer M; Butt L; Hemachandra LPM; Schujman S; Tokranova N; Khoury J; Papa Rao S, Characterization and Neutral Atom Beam Surface Modification of a Clear Castable Polyurethane for Biomicrofluidic Applications. Surfaces 2019, 2 (1), 100–116.
36. Hwang G; Yang J-H; Lee C-H; Ahn I-S; Mhin BJ, New Selection Criterion for a Base Polar Liquid in the Lifshitz–van der Waals/Lewis Acid–Base approach. The Journal of Physical Chemistry C 2011, 115 (25), 12458–12463.
37. Hwang G; Ahn I-S; Mhin BJ; Kim J-Y, Adhesion of Nano-sized Particles to the Surface of Bacteria: Mechanistic Study with the Extended DLVO Theory. Colloids and Surfaces B: Biointerfaces 2012, 97, 138–144. [PubMed: 22609594]
38. Hwang G; Lee C-H; Ahn I-S; Mhin BJ, Analysis of the Adhesion of Pseudomonas putida NCIB 9816-4 to a Silica Gel as a Model Soil using Extended DLVO Theory. Journal of Hazardous Materials 2010, 179 (1-3), 983–988. [PubMed: 20399555]
39. Rulison C So You Want to Measure Surface Energy; 1999; pp 1–16.
40. Król P; Lechowicz JB; Król B, Modelling the Surface Free Energy Parameters of Polyurethane Coats—Part 1. Solvent-based Coats Obtained from Linear Polyurethane Elastomers. Colloid and polymer science 2013, 291 (4), 1031–1047. [PubMed: 23525512]
41. Collins L; Kilpatrick JI; Vlassiouk IV; Tselev A; Weber SA; Jesse S; Kalinin SV; Rodriguez BJ, Dual Harmonic Kelvin Probe Force Microscopy at the Graphene–liquid Interface. Applied physics letters 2014, 104 (13), 133103, 1–5.
42. van Oss CJ, The Extended DLVO Theory. In Interface Science and Technology, Elsevier: 2008; Vol. 16, pp 31–48.
43. Hermanowicz P; Sarna M; Burda K; Gabryś H, AtomicJ: An Open Source Software for Analysis of Force Curves. Rev. Sci. Instrum. 2014, 85 (6), 063703, 1–8. [PubMed: 24985823]
44. ISO 4049: 2019 — Dentistry — Polymer-based Restorative Materials. 5 ed.; International Standards Organization: Geneva, Switzerland, 2019.
45. Zumdahl SS; Zumdahl SA; DeCoste DJ, Chemistry: An Atoms First Approach. Cengage Learning: 2020.
46. Frey M; Payne D, Grain-size Effect on Structure and Phase Transformations for Barium Titanate. Physical Review B 1996, 54 (5), 3158.

47. McNeal MP; Jang S-J; Newnham RE, The Effect of Grain and Particle Size on the Microwave Properties of Barium Titanate (BaTiO 3). Journal of applied Physics 1998, 83 (6), 3288–3297.
48. Zhao Z; Buscaglia V; Viviani M; Buscaglia MT; Mitoseriu L; Testino A; Nygren M; Johnsson M; Nanni P, Grain-size Effects on the Ferroelectric Behavior of Dense Nanocrystalline BaTiO 3 Ceramics. Physical Review B 2004, 70 (2), 024107, 1–8.
49. ISO 25178-2: 2012 — Geometrical Product Specifications (GPS) — Surface Texture: Areal — Part 2: Terms, Definitions and Surface Texture Parameters. International Standards Organization: Geneva, Switzerland, 2012.
50. Tokuda K; Ogino T; Kotera M; Nishino T, Simple Method for Lowering Poly (methyl methacrylate) Surface Energy with Fluorination. Polymer Journal 2015, 47 (1), 66–70.
51. Dorranian D; Abedini Z; Hojabri A; Ghoranneviss M, Structural and Optical Characterization of PMMA Surface Treated in Low Power Nitrogen and Oxygen RF Plasmas. Journal of Non-Oxide Glasses 2009, 1 (3), 217–229.
52. Sharma P; Rao KH, Analysis of different approaches for evaluation of surface energy of microbial cells by contact angle goniometry. Advances in Colloid and Interface Science 2002, 98 (3), 341–463. [PubMed: 12206199]
53. Bos R; Van der Mei HC; Busscher HJ, Physico-chemistry of Initial Microbial Adhesive Interactions–its Mechanisms and Methods for Study. FEMS microbiology reviews 1999, 23 (2), 179–230. [PubMed: 10234844]
54. Roberts S, Dielectric and Piezoelectric Properties of Barium Titanate. Physical Review 1947, 71 (12), 890.
55. Acosta M; Novak N; Rojas V; Patel S; Vaish R; Koruza J; Rossetti GA Jr; Rödel J, BaTiO3-based Piezoelectrics: Fundamentals, Current Status, and Perspectives. Applied Physics Reviews 2017, 4 (4), 041305, 1–53.
56. Randolph LD; Palin WM; Leloup G; Leprince JG, Filler Characteristics of Modern Dental Resin Composites and their Influence on Physico-mechanical Properties. Dental Materials 2016, 32 (12), 1586–1599. [PubMed: 27720423]
57. Tahayeri A; Morgan M; Fugolin AP; Bompolaki D; Athirasala A; Pfeifer CS; Ferracane JL; Bertassoni LE, 3D Printed versus Conventionally Cured Provisional Crown and Bridge Dental Materials. Dental Materials 2018, 34 (2), 192–200. [PubMed: 29110921]
58. Zhao J; Ghannam R; Htet KO; Liu Y; Law MK; Roy VA; Michel B; Imran MA; Heidari H, Self-Powered Implantable Medical Devices: Photovoltaic Energy Harvesting Review. Advanced Healthcare Materials 2020, 9 (17), 2000779, 1–22.
59. Hsu BB; Park M-H; Hagerman SR; Hammond PT, Multimonth Controlled Small Molecule Release from Biodegradable Thin Films. Proceedings of the National Academy of Sciences 2014, 111 (33), 12175–12180.
60. Xu D; Su Y; Zhao L; Meng F; Liu C; Guan Y; Zhang J; Luo J, Antibacterial and Antifouling Properties of a Polyurethane Surface Modified with Perfluoroalkyl and Silver Nanoparticles. Journal of Biomedical Materials Research Part A 2017, 105 (2), 531–538. [PubMed: 27737518]
61. Sharma S; Jaimes-Lizcano YA; McLay RB; Cirino PC; Conrad JC, Subnanometric Roughness Affects the Deposition and Mobile Adhesion of Escherichia coli on Silanized Glass Surfaces. Langmuir 2016, 32 (21), 5422–5433. [PubMed: 27158837]
62. Truong VK; Lapovok R; Estrin YS; Rundell S; Wang JY; Fluke CJ; Crawford RJ; Ivanova EP, The Influence of Nano-scale Surface Roughness on Bacterial Adhesion to Ultrafine-grained Titanium. Biomaterials 2010, 31 (13), 3674–3683. [PubMed: 20163851]
63. Cheng Y; Feng G; Moraru CI, Micro-and Nanotopography Sensitive Bacterial Attachment Mechanisms: A Review. Frontiers in microbiology 2019, 10, 191. [PubMed: 30846973]
64. Lassila LV; Garoushi S; Tanner J; Vallittu PK; Söderling E, Adherence of Streptococcus mutans to Fiber-reinforced Filling Composite and Conventional Restorative materials. The open dentistry journal 2009, 3, 227. [PubMed: 20148170]
65. Van der Mei H; de Soet J; de Graaff J; Rouxhet P; Busscher H, Comparison of the Physicochemical Surface Properties of Streptococcus rattus with those of Other mutans Streptococcal Species. Caries research 1991, 25 (6), 415–423. [PubMed: 1810653]

66. Metwally S; Stachewicz U, Surface Potential and Charges Impact on cell Responses on Biomaterials Interfaces for Medical Applications. Materials Science and Engineering: C 2019, 104, 109883. [PubMed: 31500046]

67. Ding X; Xu S; Li S; Guo Z; Lu H; Lai C; Wu J; Wang J; Zeng S; Lin X, Biological Effects of Titanium Surface Charge with a Focus on Protein Adsorption. ACS omega 2020, 5 (40), 25617–25624. [PubMed: 33073087]

68. Xu L-P; Meng J; Zhang S; Ma X; Wang S, Amplified Effect of Surface Charge on Cell Adhesion by Nanostructures. Nanoscale 2016, 8 (25), 12540–12543. [PubMed: 27150434]

69. Bacakova L; Filova E; Parizek M; Ruml T; Svorcik V, Modulation of Cell Adhesion, Proliferation and Differentiation on Materials Designed for Body Implants. Biotechnol. Adv 2011, 29 (6), 739–767. [PubMed: 21821113]

70. Tripathy SS; Raichur AM, Dissolution Properties of BaTiO3 Nanoparticles in Aqueous Suspensions. Journal of Experimental Nanoscience 2011, 6 (2), 127–137.

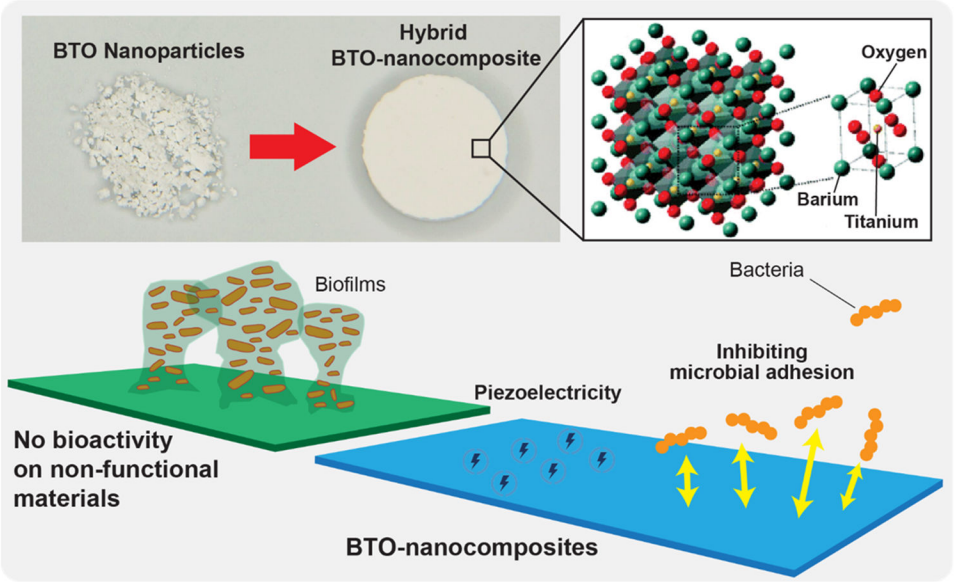

Figure 1.
Schematic diagram of bimodal BTO-nanocomposites biomaterial platform with antibiofilm and self-powering functionalities.

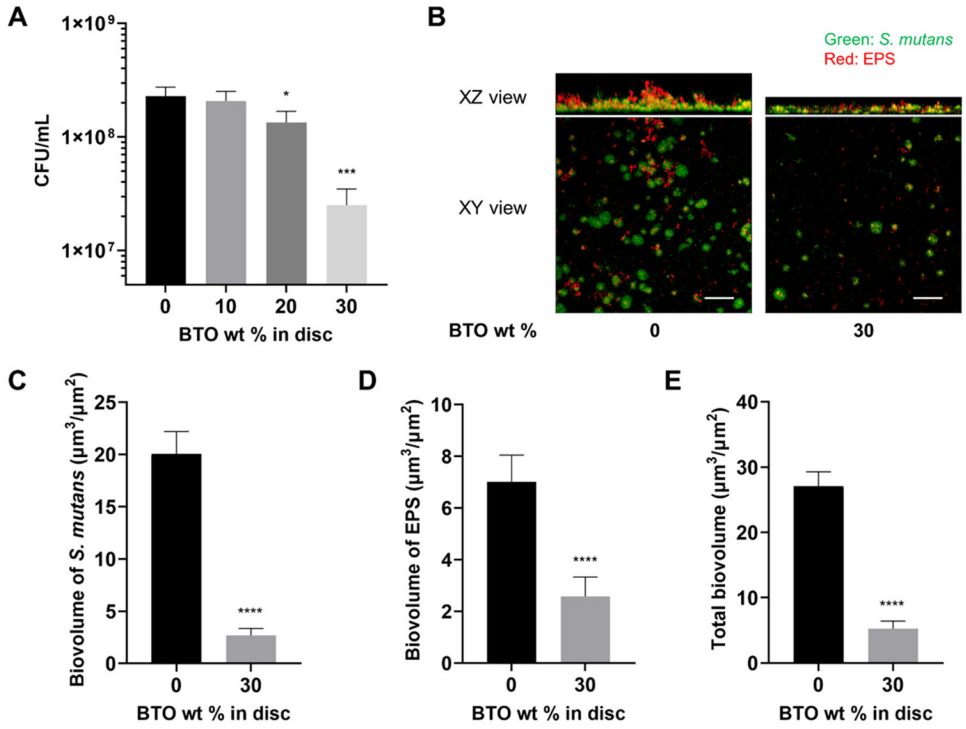

Figure 2.

Antibiofilm activity of BTO-nanocomposite discs. (A) Dose-dependent reduction in CFU/mL with increasing wt% of BTO in discs. Data represent means. Error bars are standard deviations. Statistics: One-way ANOVA: $p < 0.001$. Post-hoc (Dunnett's method): *** represents $p < 0.001$ in comparison to control discs (0 wt%) (n=3). (B) Representative top (XY) and orthogonal (XZ) views of confocal images of *S. mutans* biofilms at 18 h for control discs (0 wt%) and 30 wt% BTO-nanocomposite discs. Bacterial microcolonies were labeled with SYTO 9 (green) and EPS α-glucan were labeled with Alexa Fluor 647 (red). Scale bar: 50 μm. Quantified biovolume of (C) *S. mutans*, (D) EPS, and (E) total (sum of *S. mutans* and EPS) in the biofilm as determined by COMSTAT. Data represent means. Error bars are standard deviations. Statistics: t-test with **** representing $p < 0.0001$ (n≥3).

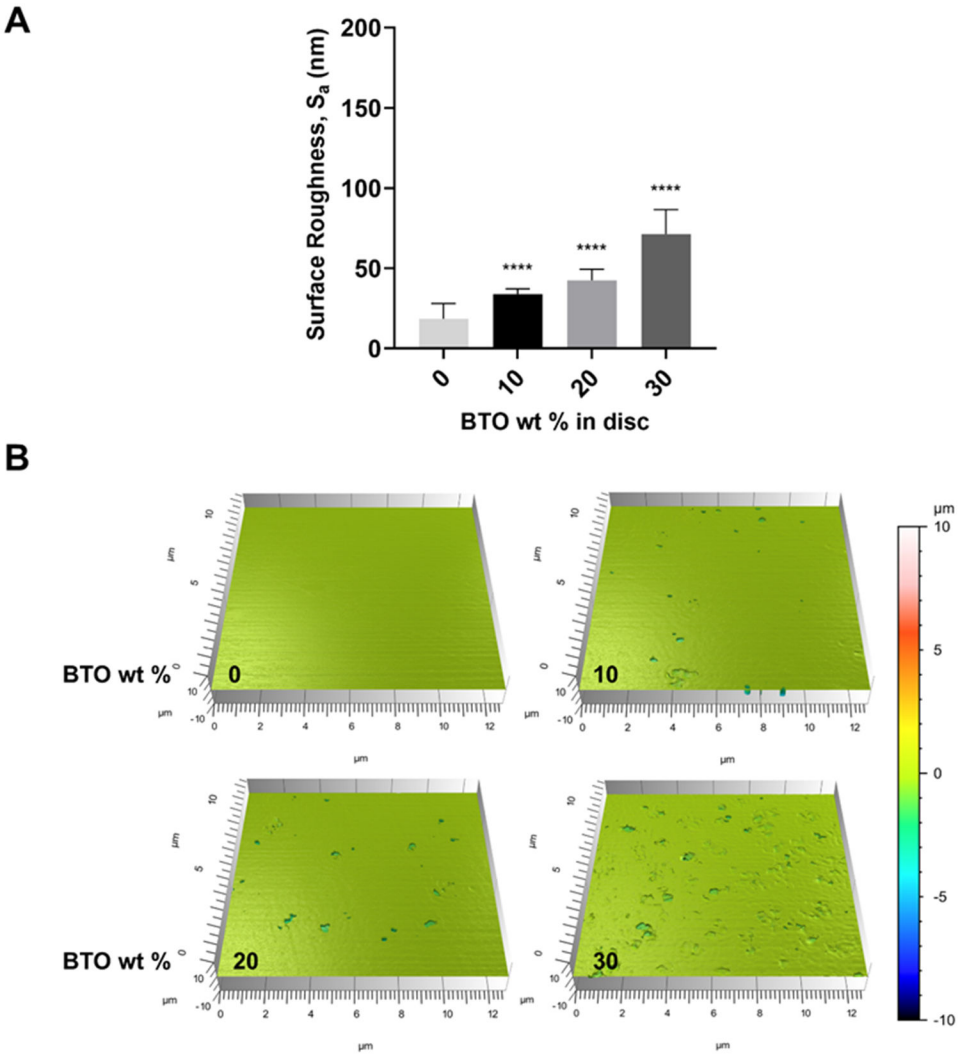

Figure 3.

Surface roughness of control and BTO-nanocomposite discs. (A) Quantified surface roughness values of control and BTO-nanocomposite discs. The data show a dose-dependent increase in surface roughness (arithmetical mean height values, S_a) for increasing wt% of BTO in discs. Data represent means. Error bars are standard deviations. Statistics: One-way ANOVA: $p < 0.0001$. Post-hoc (Dunnett's method): **** represents $p < 0.0001$ in comparison to control discs (0 wt%). (B) Representative 3D topographical scans (12.8 µm x 12.8 µm scans; 10 random spots per disc) for discs with varying BTO wt% (n≥3).

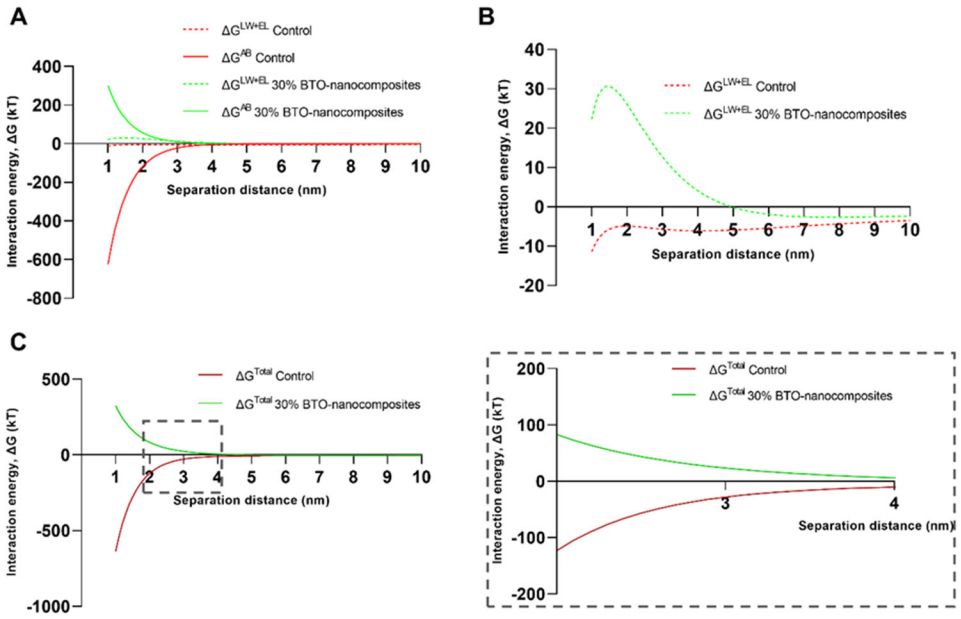

Figure 4.

Interaction energy profiles between *S. mutans* and discs. (A) Modeled components of the total interaction energy (ΔG) from the xDLVO theory (LW: Lifshitz–van der Waals interactions; EL: electrostatic interactions; AB: Lewis acid-base interactions) for control and 30 wt% BTO-nanocomposite discs. (B) Energy profiles of the sum of LW and EL (DLVO components) depict a larger repulsive energy barrier for interaction between *S. mutans* and 30 wt% BTO-nanocomposite discs. (C) Total interaction energy (LW+EL+AB) for control and 30 wt% BTO-nanocomposite discs. Inset depicts a magnification of the profiles between separation distances of 2 to 4 nm (n≥3).

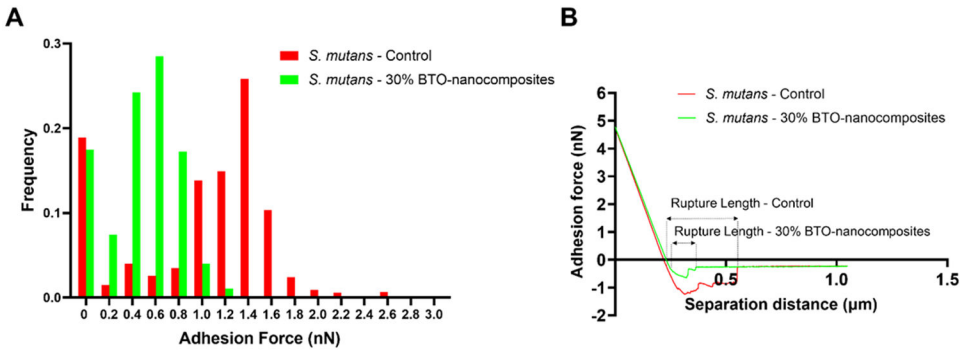

Figure 5.

Binding forces between *S. mutans* and discs. (A) Frequency distributions for adhesion forces between *S. mutans* - control discs and *S. mutans* - 30 wt% BTO-nanocomposite discs using sc-AFM. Distributions represent 1200 force curves from 10 x 10 force maps. Adhesion forces for *S. mutans* - control discs were 2.25-fold higher than for *S. mutans* - 30 wt% BTO-nanocomposite discs. (B) Representative adhesion force curves between *S. mutans*-control discs and *S. mutans*-30 wt% BTO-nanocomposite discs indicating a longer and "stickier" rupture of the interaction between *S. mutans* - control than *S. mutans* - BTO-nanocomposite discs (n≥3).

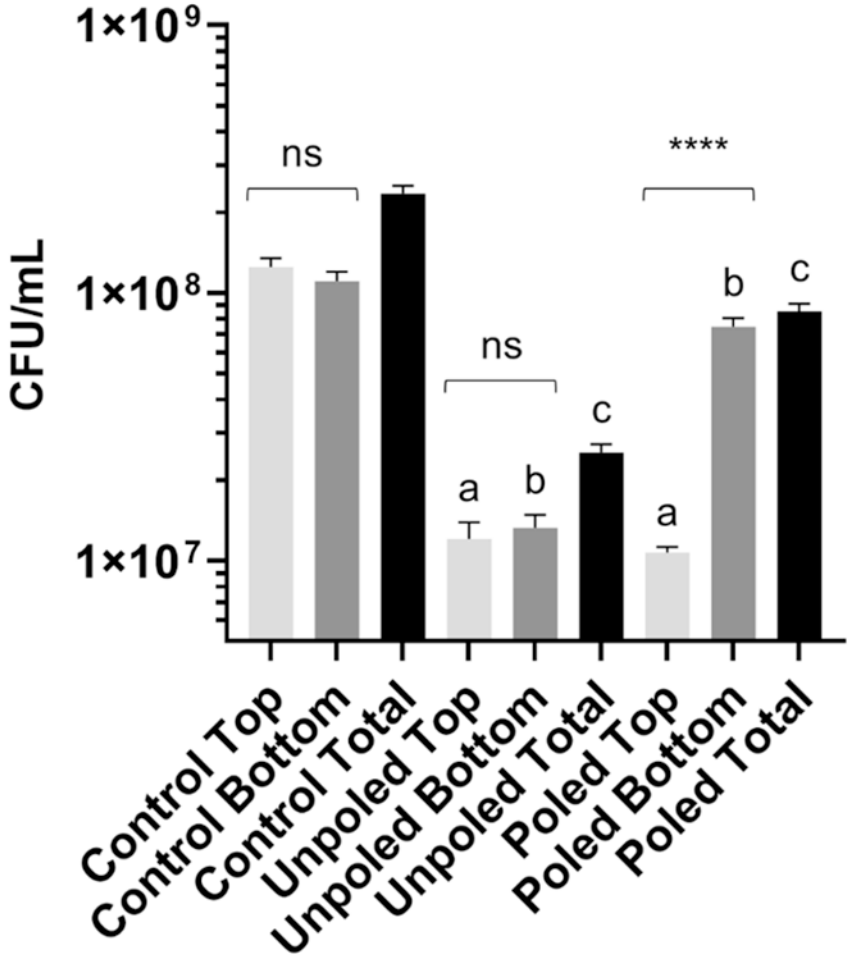

Figure 6.

Antibiofilm activity of separate surfaces of poled and unpoled BTO-nanocomposite discs. Data represent means. Error bars are standard deviations. Statistics: One-way ANOVA: $p < 0.0001$. Post-hoc: ‘a’, ‘b’ and ‘c’ represent $p < 0.0001$ in comparison to control for top, bottom, and total, respectively; top and bottom surfaces within each condition are compared by * marks (n=3).

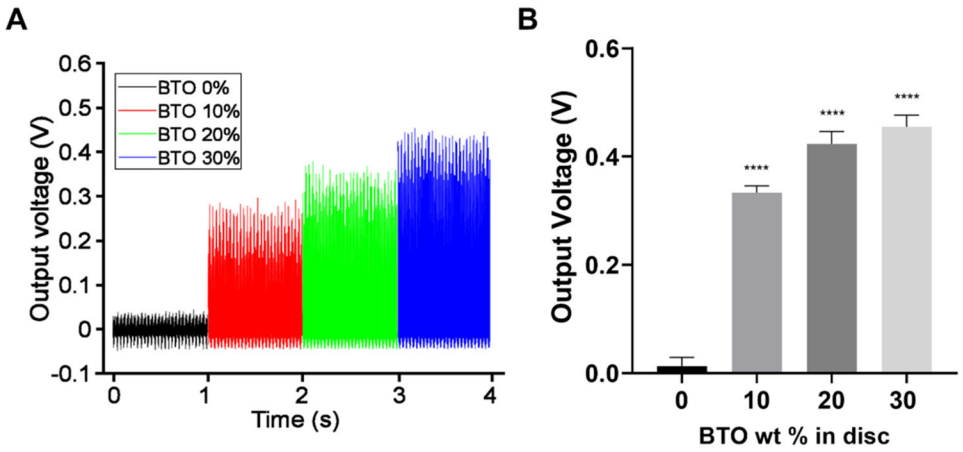

Figure 7.

Piezoelectric output voltages for BTO-nanocomposite discs. Piezoelectric output increases with increasing BTO concentration in the composites: (A) measured voltage output under mechanical stimulation and (B) averaged voltage output as a function of BTO concentration. Data represent means. Errors bars are standard deviations. Statistics: One-way ANOVA: $p < 0.0001$. Post-hoc (Dunnett's method): **** represents $p < 0.0001$ in comparison to control discs (0 wt%) (n≥3).

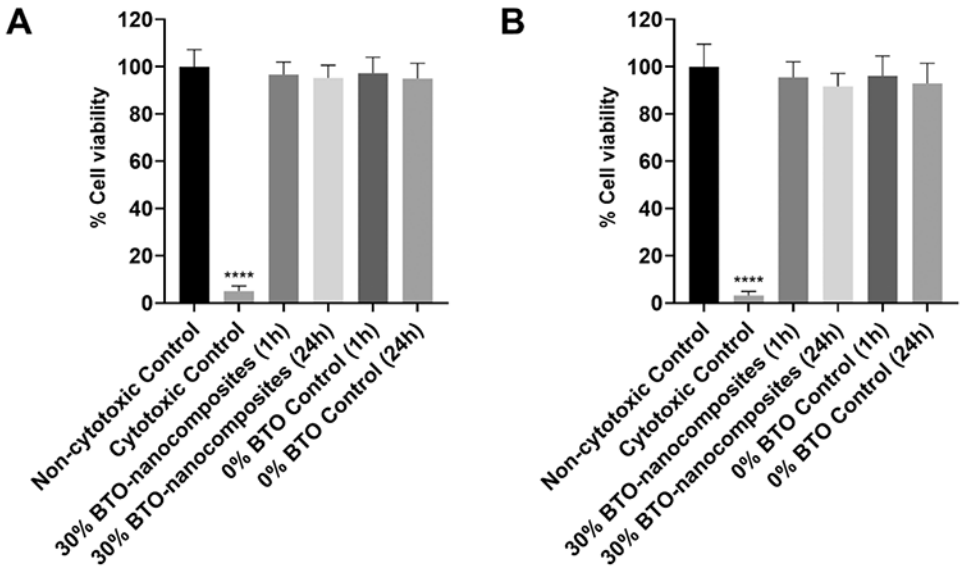

Figure 8.

Cytotoxicity of discs towards HGFs and HGKs. Percentage cell viability for extract test-based cytotoxic screening of control and 30 wt% BTO-nanocomposite discs towards (A) human gingival fibroblasts (HGFs) and (B) human gingival keratinocytes (HGKs). Neither disc had any significant cytotoxicity towards both HGFs and HGKs. Data represent means. Error bars are standard deviations. Statistics: One-way ANOVA: $p < 0.001$. Post-hoc (Dunnett's method): **** represents $p < 0.0001$ in comparison to negative control (n≥3).